

Nonequilibrium quantum systems with electron-phonon interactions: Transient dynamics and approach to steady state

Eli Y. Wilner,¹ Haobin Wang,² Michael Thoss,³ and Eran Rabani⁴

¹*School of Physics and Astronomy, The Sackler Faculty of Exact Sciences, Tel Aviv University, Tel Aviv 69978, Israel*

²*Department of Chemistry and Biochemistry, New Mexico State University, Las Cruces, NM 88003, USA*

³*Institute for Theoretical Physics and Interdisciplinary Center for Molecular Materials,*

Friedrich-Alexander-Universität Erlangen-Nürnberg, Staudtstr. 7/B2, 91058 Erlangen, Germany

⁴*School of Chemistry, The Sackler Faculty of Exact Sciences, Tel Aviv University, Tel Aviv 69978, Israel*

The nonequilibrium dynamics of a quantum dot with electron-phonon interactions described by a generalized Holstein model is presented. A combination of methodologies including the reduced density matrix formalism, the multilayer multiconfiguration time-dependent Hartree method, and a time-dependent nonequilibrium Green function approach, is used to explore the transient behavior on multiple timescales as the system approaches steady-state. The dot population dynamics on short to intermediate times is governed by the dot-lead hybridization parameter (Γ) and by the typical phonon frequency (ω_c) and depends on the location of the energy level of the dot relative to the bias window. At longer times, the dynamics show a distinct behavior depending on whether the system is in the adiabatic or non-adiabatic regime, with a quantum dot occupation that may depend on the initial preparation of the phonons degrees of freedom. A “phase” diagram of this localization effect as a function of the polaron shift (λ) for various phonon frequencies is derived, suggesting the existence of bistability on experimentally observable timescales.

I. INTRODUCTION

The study and understanding of nonequilibrium phenomena in many-body quantum systems has been of great interest recently. Among the variety of architectures and processes considered, energy and charge transport in nanostructures such as, e.g., single molecule junctions, carbon nanotubes, and small quantum dots have received particular attention.^{1,2} In contrast to mesoscopic or bulk systems, these nanosystems often exhibit strong electron-phonon/vibrational interactions, which manifests itself in interesting transport phenomena.^{3–6} In molecular junctions, for example, electron-phonon interaction has been shown to result in a multitude of nonequilibrium phenomena such as current-induced local heating and cooling, multistability, switching and hysteresis, as well as decoherence.^{3,7–27}

Most of the studies so far have focused on phenomena in steady-state. Much less is known about transient dynamics in nanostructures under nonequilibrium conditions. Fundamental questions to be addressed include: What are the timescales on which a steady-state is reached under nonequilibrium conditions? Which dynamical processes are of importance? What are the underlying relaxation mechanisms? What are the preconditions for the existence of a unique steady-state? In fact, the existence of a unique steady-state in many-body quantum systems with electron-phonon interaction has been a topic of great controversy in recent years.^{3,25,28–35}

In this paper, we address these questions for a generic model of charge transport in a quantum dot with electron-phonon interaction using a reduced density matrix (RDM) formalism based on projection-operator techniques.^{25,36–38} This formalism requires as input the memory kernel. To this end, we employ two different approaches: (i) a two-time nonequilibrium Green func-

tion (NEGF) method and (ii) the multilayer multiconfiguration time-dependent Hartree (ML-MCTDH)^{39,40} approach. The latter approach provides a numerically exact treatment of the nonequilibrium dynamics within a certain timescale. Because the memory kernel decays typically on a much shorter timescale than the RDM matrix itself, this strategy allows a significant extension of the timescale accessible by numerically exact ML-MCTDH technique and by the two-time NEGF approach. This was demonstrated already in previous studies of impurity models with electron-electron^{37,38} and electron-phonon²⁵ interactions.

It should be noted that a variety of other approaches have been developed and applied to study transient phenomena in nonequilibrium quantum systems with electron-phonon interaction, including approximate methods such as master equation methods,^{41–43} as well as numerically exact schemes, such as numerical path-integral approaches^{44–46} and the scattering state numerical renormalization group technique.⁴⁷ The approaches employed in the present work allow a significant extension of such studies with respect to the complexity of the phonon bath, the range of physical parameters, and the accessible timescales.

The remainder of the paper is organized as follows. The model and the theoretical methodology is outlined in Sec. II. In Sec. III, we analyze the quantum dynamics, in particular with respect to the different timescales inherent in the transient dynamics and the approach to steady-state. The dependence of the dynamics on the initial preparation is discussed in Sec. IV. Sec. V concludes with a summary.

II. MODEL AND THEORETICAL FRAMEWORK

A. Model Hamiltonian

We consider a generic model for charge transport through a quantum dot with electron-phonon interaction, often referred to as the extended nonequilibrium Holstein model. The model is described by the Hamiltonian:

$$H = H_S + H_B + V_{SB} \quad (1)$$

where

$$H_S = \varepsilon_d d^\dagger d \quad (2)$$

is the system (quantum dot) Hamiltonian, comprising a single electronic state with energy ε_d and corresponding fermionic creation/annihilation operators d^\dagger/d . The bath is described by the sum of fermionic leads and bosonic modes, $H_B = H_\ell + H_{\text{ph}}$, where

$$H_\ell = \sum_{k \in L, R} \varepsilon_k a_k^\dagger a_k \quad (3)$$

represents the noninteracting left/right (L/R) leads Hamiltonian with fermionic creation/annihilation operators a_k^\dagger/a_k . The bosonic bath Hamiltonian representing the phonons is given by:

$$H_{\text{ph}} = \sum_{\alpha} \hbar \omega_{\alpha} \left(b_{\alpha}^\dagger b_{\alpha} + \frac{1}{2} \right) \quad (4)$$

where $b_{\alpha}^\dagger/b_{\alpha}$ are the ladder operators for the phonon mode α with energy $\hbar \omega_{\alpha}$. Finally, the coupling between the system and the baths is given by

$$V_{SB} = \sum_{k \in L, R} \left(t_k d a_k^\dagger + t_k^* a_k d^\dagger \right) + d^\dagger d \sum_{\alpha} M_{\alpha} (b_{\alpha}^\dagger + b_{\alpha}) \quad (5)$$

where t_k is the coupling strength between the system and lead state k , determined from the relation

$$\Gamma_{L,R}(\varepsilon) = 2\pi \sum_{k \in L,R} |t_k|^2 \delta(\varepsilon - \varepsilon_k). \quad (6)$$

Here, $\Gamma_{L,R}(\varepsilon) = \frac{a^2}{b^2} \sqrt{4b^2 - (\varepsilon - \mu_{L,R})^2}$ is the electron spectral density, which is assumed to be of tight-binding form, and $\mu_{L,R}$ is the chemical potential of the left/right lead, respectively. In the applications reported below we choose typical parameters for a metal lead, namely, $a = 0.2\text{eV}$ and $b = 1\text{eV}$. For convenience the results in this paper are mostly presented in dimensionless units scaled by Γ , where $\Gamma = 0.16\text{eV}$ is the maximum value of $\Gamma_R(\varepsilon) + \Gamma_L(\varepsilon)$.

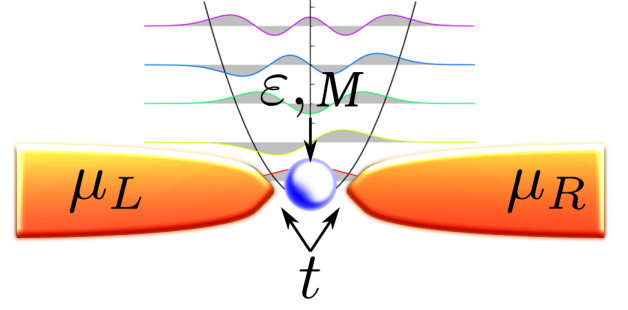


Figure 1: A sketch of the quantum dot coupled to left and right leads and to a phonon bath.

The second term in Eq. (5) represents the electron-phonon coupling, where M_{α} is the coupling strength to mode α determined from the relation

$$J(\omega) = \pi \sum_{\alpha} M_{\alpha}^2 \delta(\hbar\omega - \hbar\omega_{\alpha}) \quad (7)$$

where $J(\omega) = \frac{\pi\hbar}{2} \eta \omega e^{-\frac{\omega}{\omega_c}}$ is the phonon spectral function assumed to be of Ohmic form. The dimensionless Kondo parameter, $\eta = \frac{2\lambda}{\hbar\omega_c}$, determines the overall strength of the electron-phonon couplings, where ω_c is the characteristic phonon bath frequency and $\lambda = \sum_{\alpha} \frac{M_{\alpha}^2}{\hbar\omega_{\alpha}} = \frac{1}{\pi} \int \frac{d\omega}{\omega} J(\omega)$ is the reorganization energy (or polaron shift), which also determines the shifting of the dot energy upon charging. We set realistic relaxation timescales for the phonon bath, *i.e.*, by choosing its characteristic frequency, ω_c , in the range of $25 - 1000\text{cm}^{-1}$, which is $\approx 0.02 - 0.8$ in units of Γ/\hbar .

The model introduced above and variants thereof have been widely used to study nonequilibrium charge transport in nanostructures, such as, for example, semiconductor quantum dots,⁴⁸ carbon nanotubes⁴ or molecular junctions.^{3,7,49-52} In the latter case, the phonons may include, in addition to the phonons of the contacts, the vibrational degrees of freedom of the molecule.

B. Reduced density matrix formalism

To study the dynamic response on multiple timescales generated by the extended Holstein model as the system is driven away from equilibrium, we adopt the reduced density matrix (RDM) formalism³⁸ discussed in detail in Ref. 37) for the Anderson impurity model and in Ref. 25 for the present model. The equation of motion for the RDM, $\sigma(t) = \text{Tr}_B\{\rho(t)\}$, is given by

$$i\hbar \frac{\partial}{\partial t} \sigma(t) = \mathcal{L}_S \sigma(t) + \vartheta(t) - \frac{i}{\hbar} \int_0^t d\tau \kappa(\tau) \sigma(t - \tau) \quad (8)$$

where $\mathcal{L}_S = [H_S, \dots]$ is the system's Liouvillian, $\text{Tr}_B\{\dots\}$ is a trace over the baths degrees of freedom (leads and phonon baths) and $\rho(t)$ is the full density matrix which obeys the von-Neuman equation of motion. In

the above,

$$\vartheta(t) = \text{Tr}_B \left\{ \mathcal{L}_V e^{-\frac{i}{\hbar} Q \mathcal{L} t} Q \rho(0) \right\} \quad (9)$$

depends on the choice of initial conditions and $\mathcal{L}_v = [V_{SB}, \dots]$. By construction, $\vartheta(t)$ vanishes for an uncorrelated initial state, *i.e.* when $\rho(0) = \sigma(0) \otimes \rho_B(0)$, where $\sigma(0)$ and $\rho_B(0)$ are the system and baths initial density matrices, respectively. In all applications reported below we start from a factorized initial condition and thus, ignore $\vartheta(t)$. The memory kernel, which describes the non-Markovian dependency of the time propagation of the system, is given by

$$\kappa(t) = \text{Tr}_B \left\{ \mathcal{L}_V e^{-\frac{i}{\hbar} Q \mathcal{L} t} Q \mathcal{L} \rho_B \right\} \quad (10)$$

where $Q = 1 - P$, $P = \rho_B(0) \text{Tr}_B \{\dots\}$ is a projection operator, and $\mathcal{L} = [H, \dots]$ is the full Liouvillian super-operator.

To obtain $\sigma(t)$, one requires as input the super-matrix of the memory kernel. For a general system the super-matrix has N^4 elements, where N is the dimension of the density matrix. Thus, calculating all elements can be a tedious task.³⁷ The complexity is considerably reduced for the extended Holstein model. First, $N = 2$ and hence the memory kernel has only 16 terms. Second, the reduced dynamics of the diagonal elements of $\sigma(t)$ (the populations) are decoupled from those of the off-diagonal elements (the coherences). If one is interested in the populations alone (as is the case in the present study), only 4 elements of the memory kernel are necessary to describe the population dynamics. To further simplify the calculations of the memory, we express it in terms of a Volterra equation of the second type, removing the complexity of the projected dynamics of Eq. (10):

$$\kappa(t) = i\hbar \dot{\Phi}(t) - \Phi(t) \mathcal{L}_S + \frac{i}{\hbar} \int_0^t d\tau \Phi(t - \tau) \kappa(\tau) \quad (11)$$

with

$$\Phi(t) = \text{Tr}_B \left\{ \mathcal{L}_V e^{-\frac{i}{\hbar} \mathcal{L} t} \rho_B \right\}. \quad (12)$$

Since the operator \mathcal{L}_V appearing in the equation for $\Phi(t)$ and the full Hamiltonian conserve the total particle number, only the diagonal matrix elements $\Phi(t)$ need to be computed:

$$\Phi_{nn,mm}(t) = \frac{2}{\hbar} \text{Tr}_B \left\{ \rho_B \langle m | \sum_k t_k d(t) a_k^\dagger(t) | m \rangle \right\} .. \quad (13)$$

Here, $|m\rangle$ denotes the electronic state of the quantum dot, where m can take the values 1 or 0, corresponding to an occupied or an unoccupied dot, respectively. Note that $\Phi_{nn,mm}(t)$ is independent on n and thus has only 2 independent components. The above expression for $\Phi_{nn,mm}(t)$ has a simple physical interpretation as the

time derivative of the dot population and can be expressed in terms of the sum of the left ($I_m^L(t)$) and right ($I_m^R(t)$) currents:

$$e\Phi_{nn,mm}(t) = I_m^L(t) + I_m^R(t), \quad (14)$$

where

$$I_m^{L,R}(t) = -\frac{2e}{\hbar} \Im \sum_{k \in L,R} t_k \langle m | d(t) a_k^\dagger(t) | m \rangle, \quad (15)$$

is the left/right current for an initial occupied ($m = 1$) or empty ($m = 0$) dot, and e is the electron charge.

C. Calculation of the Memory Kernel

The RDM formalism may seem redundant, since in order to obtain the reduced density matrix one requires as input the memory kernel which is given in terms of the left and right currents. If the left and right currents are accessible by impurity solvers, so are the elements of the RDM. This, however, ignores the fact that the memory kernel typically decays on a much faster timescale compared to the RDM itself.^{25,37,38} Thus, if the memory decays to zero at $t > t_c$ where t_c is a cutoff time, it is sufficient to obtain the memory kernel to t_c and infer from that the dynamics of the RDM at all times. We refer to this as the ‘‘cutoff approximation’’, which will become exact if the memory kernel has a finite range and decays to zero at $t > t_c$. Since numerical solvers of quantum impurity models scale exponentially with the propagation time, this saves significant computational time. As will be shown below, the RDM formalism provides means to study the dynamics on timescales not accessible by direct impurity solvers.^{25,53}

We adopt two impurity solvers to calculate the memory kernel. The first is based on the so-called multilayer multiconfiguration time-dependent Hartree theory in second quantization representation (ML-MCTDH-SQR)⁴⁰ and the second, described below, is based on a two-time nonequilibrium Green function (NEGF) formalism.

1. Multilayer multiconfiguration time-dependent Hartree (ML-MCTDH) theory

The ML-MCTDH theory is a rigorous variational method used for propagating wave packets in complex systems with many degrees of freedom.³⁹ Extending the original MCTDH method,^{54,55} employs a hierarchical, multilayer representation of the many-body wave function. Originally developed for treating distinguishable particles, it has recently been generalized to describe indistinguishable fermionic or bosonic particles employing occupation number representation of the Fock space in the second quantized framework.⁴⁰ The approach has

been applied to nonequilibrium transport with electron-phonon^{33,40,56,57} and electron-electron interactions.⁵⁸ For completeness, we provide a brief summary of this approach and its specific implementation for calculating the memory kernel in the extended Holstein model.

Within the ML-MCTDH, the wave function is represented by a recursive, layered expansion

$$|\Psi(t)\rangle = \sum_{j_1} \sum_{j_2} \cdots \sum_{j_p} A_{j_1 j_2 \dots j_p}(t) \prod_{\kappa=1}^p |\varphi_{j_\kappa}^{(\kappa)}(t)\rangle \quad (16)$$

$$|\varphi_{j_\kappa}^{(\kappa)}(t)\rangle = \sum_{i_1} \sum_{i_2} \cdots \sum_{i_{Q(\kappa)}} B_{i_1 i_2 \dots i_{Q(\kappa)}}^{\kappa, j_\kappa}(t) \prod_{q=1}^{Q(\kappa)} |v_{i_q}^{(\kappa, q)}(t)\rangle \quad (17)$$

$$|v_{i_q}^{(\kappa, q)}(t)\rangle = \sum_{\alpha_1} \sum_{\alpha_2} \cdots \sum_{\alpha_{M(\kappa, q)}} C_{\alpha_1 \alpha_2 \dots \alpha_{M(\kappa, q)}}^{\kappa, j_\kappa, i_q}(t) \prod_{q=1}^{M(\kappa, q)} |\xi_{\alpha_\gamma}^{(\kappa, q, \gamma)}(t)\rangle \quad (18)$$

where $A_{j_1 j_2 \dots j_p}$, $B_{i_1 i_2 \dots i_{Q(\kappa)}}^{\kappa, j_\kappa}$, $C_{\alpha_1 \alpha_2 \dots \alpha_{M(\kappa, q)}}^{\kappa, j_\kappa, i_q}$ and so on are the expansion coefficients for the first, second, third, ..., layers, respectively. $|\varphi_{j_\kappa}^{(\kappa)}(t)\rangle$, $|v_{i_q}^{(\kappa, q)}(t)\rangle$, $|\xi_{\alpha_\gamma}^{(\kappa, q, \gamma)}(t)\rangle$, ..., are the single particle functions for the first, second, third, ..., layers. For distinguishable particles, the primitive basis functions for each degree of freedom in the deepest layer can be any convenient choice depending on the specific form of the Hamiltonian operator, e.g., Fourier grid points, harmonic oscillator eigenfunctions, Legendre polynomials, etc. When treating identical particles, a second quantization representation (SQR) is employed, where the primitive basis functions for each single particle group in the deepest layer are the occupation number states of this Fock subspace.⁴⁰ This is referred to as the ML-MCTDH-SQR approach. In principle, the recursive multilayer expansion/hierarchical tensor decomposition can be carried out to an arbitrary number of layers. In practice, the multilayer hierarchy is terminated at a particular level by expanding the single particle functions in the deepest layer in terms of time-independent configurations/primitive basis functions. The ML-MCTDH equations of motion are obtained by applying Dirac-Frenkel variational principle to Eq. (16).^{39,40} In the applications reported below, four dynamical layers are used to represent the wave function.

Within a certain timescale, the electronic and phonon continua can be discretized to and represented by a finite number of electronic states and phonon modes. For the parameter regimes discussed in this paper, a typical number of 300 – 400 electronic states and 800 – 1200 phonon modes were sufficient to achieve convergence (to within a few percent relative error). Systematic test-calculations

were then carried out to check against the number of primitive basis functions and the number of configurations for each layer until convergence was achieved.^{39,40} The computed time-dependent multilayer wave functions were then used to obtain the left and right currents $I_0^L(t)$, $I_1^L(t)$, $I_0^R(t)$, and $I_1^R(t)$ and the currents were used to generate the elements of $\Phi_{nn,mm}(t)$ and the corresponding elements of the memory kernel were obtained by solving the Volterra equation (cf., Eq. 11).

As an illustration of the combined RDM and ML-MCTDH-SQR approaches, in Fig. 2 we show the four elements of the memory kernel (upper panel) obtained for an extended Holstein model and the corresponding average system population (σ_{11}). The time evolution of $\sigma(t)$ clearly agrees with the direct calculation based on the ML-MCTDH-SQR result up to the cutoff time $t_c \approx 35 \frac{\hbar}{\Gamma}$. Beyond this time, it is difficult to converge the direct ML-MCTDH-SQR calculations and the RDM formalism employing the memory kernel obtained using ML-MCTDH-SQR is employed. The results obtained with the RDM formalism shows a pronounced dynamical effect beyond t_c . The inset in Fig. 2 shows the steady-state value of σ_{11} as a function of the inverse cutoff time. As $1/t_c \rightarrow 0$ we observe a plateau for σ_{11} suggesting that the memory has sufficiently decayed to 0.

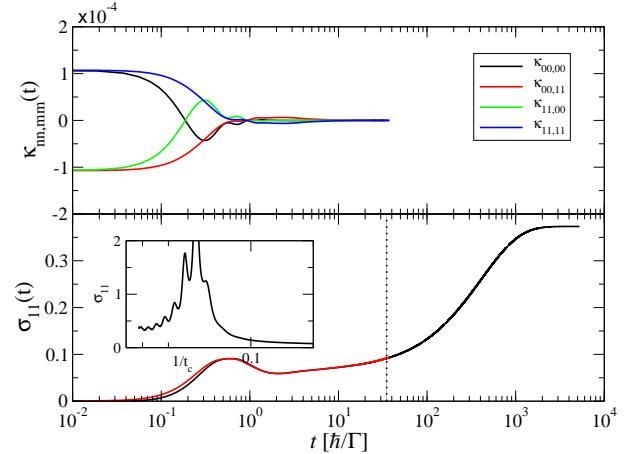


Figure 2: Upper panel: The elements of the memory kernel for the extended Holstein model for $\varepsilon_d/\Gamma = \frac{25}{8}$, $\omega_c = 500\text{cm}^{-1} \approx 0.4\Gamma/\hbar$, $\lambda/\Gamma = 3.5$, $\mu_L - \mu_R \approx \frac{5}{8}\Gamma$, and $T = 0\text{K}$. Lower panel: Corresponding values of $\sigma_{11}(t)$ obtained directly from the ML-MCTDH-SQR (red curve) and from the RDM formalism (black curve). Inset: Steady state values for σ_{11} versus $1/t_c$. The dashed vertical line shows the cutoff time.

2. Time-dependent nonequilibrium Green's function approach within the two-time self-consistent Born approximation

In situations where the calculation of the RDM does not converge within the cutoff time accessible by the ML-MCTDH-SQR approach we obtain the memory kernel from a nonequilibrium Green function approach within

the self-consistent Born approximation (SCBA). This approach is accurate only for the perturbative regime, *i.e.*, when λ/Γ is small.⁵⁰ In this regime, the NEGF-SCBA expands the cutoff time by nearly a factor of 3, thereby providing a valuable tool to converge the memory kernel and the RDM for weak electron-phonon couplings.

Most applications based on NEGF within the SCBA have addressed steady-state properties alone. Naturally, for nonequilibrium conditions one requires a two-time representation of the Green functions (GFs), significantly complicating the calculations. If one wishes to refrain from adopting any type of time-local approximation,³⁵ the two-time representation limits the timescales that can be addressed directly by the NEGF formulation. Therefore, to obtain the dynamic response on all relevant timescales, the two-time NEGF formalism must be coupled with the RDM formalism.

Here, we extended the two-time NEGF approach to calculate the time-dependent left and right currents, obtain the memory kernel and the corresponding RDM. As far as we know, the present work is also the first application of the two-time NEGF formalism to the extended Holstein model. For completeness, we provide a full description of the two-time NEGF approach. We begin by introducing contour order two-time GFs⁵⁹

$$\mathcal{G}(t, \tau) = -\frac{i}{\hbar} \langle T_c d(t) d^\dagger(\tau) \rangle \quad (19)$$

for the system, and

$$\mathcal{D}_\alpha(t, \tau) = -\frac{i}{\hbar} \langle T_c x_\alpha(t) x_\alpha(\tau) \rangle \quad (20)$$

for phonon mode α , where $x_\alpha = \frac{1}{\sqrt{2}}(b_\alpha + b_\alpha^\dagger)$ is the phonon dimensionless coordinate, and T_c is the Keldysh contour time-ordering operator. We ignore correlations between different phonon modes, *i.e.* we assume $\mathcal{D}_{\alpha\beta}(t, \tau) = -\frac{i}{\hbar} \langle T_c x_\alpha(t) x_\beta(\tau) \rangle = 0$, if $\beta \neq \alpha$. As will become apparent below, this approximation works quite well and is essential to describe a realistic size of the phonon bath within the two-time formalism. The GFs in Eqs. (19) and (20) obey the Dyson equation:

$$\begin{aligned} \mathcal{G}(t, \tau) &= \mathcal{G}_0(t - \tau) + \int_c ds_1 ds_2 \mathcal{G}_0(t - s_1) \Sigma(s_1, s_2) \mathcal{G}(s_2, \tau) \\ \mathcal{D}_\alpha(t, \tau) &= \mathcal{D}_{0\alpha}(t - \tau) + \int_c ds_1 ds_2 \mathcal{D}_{0\alpha}(t - s_1) \Pi_\alpha(s_1, s_2) \mathcal{D}_\alpha(s_2, \tau) \end{aligned} \quad (21)$$

where $\mathcal{G}_0(t)$ and $\mathcal{D}_{0\alpha}(t)$ are the bare propagators of the electronic degrees of freedom on the quantum dot and phonon mode α , respectively, evolving under $H_s + H_{ph}$, and \int_c is a time integration on the Keldysh contour. In the above, Σ and Π_α are the system and phonon self-energies, respectively. As pointed out above, we apply

the SCBA to obtain these self-energies, which correspond to a partial summation of the diagrams beyond the simpler second order approximation where each bare GF is replaced by the full propagator. A self-consistence solution is computational far more demanding, but leads to a results which is more satisfactory from a theoretical point of view. In fact, we find that the SCBA is accurate even for electron-phonon couplings of the order of $\lambda/\Gamma \approx 3$, slightly outside the perturbative regime. Within the SCBA, the system and phonon self-energies are given by

$$\Sigma(t, \tau) = \Sigma_\ell(t - \tau) + i\hbar \sum_\alpha M_\alpha^2 \mathcal{D}_\alpha(t, \tau) \mathcal{G}(t, \tau) \quad (22)$$

and

$$\Pi_\alpha(t, \tau) = -i\hbar M_\alpha^2 \mathcal{G}(t, \tau) \mathcal{G}(\tau, t), \quad (23)$$

respectively. In the above expression, we neglected virtual processes coupling different phonon modes contributing to the self-energies. $\Sigma_\ell(t) = \Sigma_{\ell,L}(t) + \Sigma_{\ell,R}(t)$ represents the self-energy arising from the coupling to the leads, with retarded ('r') and lesser ('<') self-energies defined by $i\Sigma_{\ell,L/R}^r(t) = \frac{1}{2\pi} \int \Gamma_{L/R}(\varepsilon) e^{-\frac{i}{\hbar}\varepsilon t} d\varepsilon$ and $i\Sigma_{\ell,L/R}^<(t) = -\frac{1}{2\pi} \int \Gamma_{L/R}(\varepsilon) f(\varepsilon - \mu_{L/R}) e^{-\frac{i}{\hbar}\varepsilon t} d\varepsilon$, respectively, and $f(\varepsilon)$ is the Fermi-Dirac distribution. These Keldysh GFs and self-energies are obtained using Langreth rules.^{60,61}

Once the expressions for the self-energies are given, we seek a solution for the two-time GFs. Instead of solving the usual Dyson equations, a simple Leibniz rule can be applied to reduce these equations to the Kadanoff-Baym form.⁶¹⁻⁶³ For the retarded GFs, this reads

$$\begin{aligned} i\hbar \frac{\partial \mathcal{G}^r(t, \tau)}{\partial t} &= \delta(t - \tau) + \varepsilon_d \mathcal{G}^r(t, \tau) \\ &+ \int_\tau^t \Sigma^R(t, s) \mathcal{G}^r(s, \tau) ds, \end{aligned} \quad (24)$$

$$\begin{aligned} \frac{\partial^2 \mathcal{D}_\alpha^r(t, \tau)}{\partial t^2} &= -\frac{2\omega_\alpha}{\hbar} \delta(t - \tau) - \omega_\alpha^2 \mathcal{D}_\alpha^r(t, \tau) \\ &- \frac{2\omega_\alpha}{\hbar} \int_\tau^t \Pi_\alpha^r(t, s) \mathcal{D}_\alpha^r(s, \tau) ds \end{aligned} \quad (25)$$

and for the lesser GFs one finds:

$$\begin{aligned} i\hbar \frac{\partial \mathcal{G}^<(t, \tau)}{\partial t} &= \varepsilon_d \mathcal{G}^<(t, \tau) + \int_0^t \Sigma^r(t, s) \mathcal{G}^<(s, \tau) ds \\ &+ \int_0^\tau \Sigma^<(t, s) (\mathcal{G}^r(\tau, s))^\dagger ds, \end{aligned} \quad (26)$$

$$\begin{aligned} \frac{\partial^2 \mathcal{D}_\alpha^<(t, \tau)}{\partial t^2} &= -\omega_\alpha^2 \mathcal{D}_\alpha^<(t, \tau) \\ &- \frac{2\omega_\alpha}{\hbar} \int_0^t \Pi_\alpha^r(t, s) \mathcal{D}_\alpha^<(s, \tau) ds \\ &- \frac{2\omega_\alpha}{\hbar} \int_0^\tau \Pi_\alpha^<(t, s) (\mathcal{D}_\alpha^r(\tau, s))^\dagger ds. \end{aligned} \quad (27)$$

The left and right currents can be obtained from the Meir-Wingreen formula⁶⁴:

$$I_m^{L,R}(t) = -\frac{2e}{\hbar} \Im \left\{ \int_0^t \mathcal{G}^<(t,s) i\Sigma_{\ell,L/R}^r(t-s) ds + \int_0^t \mathcal{G}^r(t,s) i\Sigma_{\ell,L/R}^<(t-s) ds \right\}. \quad (28)$$

Here m denotes the dependence on the initial preparation, which enters through the initial values taken for $\mathcal{G}_0^<(0) = -\frac{i}{\hbar} \langle m | d^\dagger(0) d(0) | m \rangle = -\frac{i}{\hbar} \cdot m$.

D. Initial conditions

To characterize the population dynamics, we must define the initial condition for the full density matrix of the system and bath. To simplify the description within the RDM formalism, we start with a factorized initial condition, which implies that $\vartheta(t)$ in Eq. (9) vanishes for all times. The initial density matrix, $\rho(0)$, is given by

$$\rho(0) = \sigma(0) \otimes \rho_B(0) = \sigma(0) \otimes \rho_{\text{ph}}(0) \otimes \rho_\ell^L(0) \otimes \rho_\ell^R(0), \quad (29)$$

where $\sigma(0)$ determines whether the electronic level is initially occupied/unoccupied,

$$\rho_\ell^{L/R}(0) = \exp \left[-\beta \left(\sum_{k \in L/R} (\varepsilon_k - \mu_{L/R}) a_k^\dagger a_k \right) \right], \quad (30)$$

is the initial density matrix for the leads, and

$$\rho_{\text{ph}}(0) = \exp \left[-\beta \left\{ \sum_\alpha \hbar\omega_\alpha \left(b_\alpha^\dagger b_\alpha + \frac{1}{2} \right) + \sum_\alpha \delta_\alpha M_\alpha (b_\alpha^\dagger + b_\alpha) \right\} \right] \quad (31)$$

represents the initial density matrix of the phonon bath. In the above equations $\beta = \frac{1}{k_B T}$ is the inverse temperature.

The calculation of the different elements of the memory kernel require the calculation of the current for different initial occupation of the system ($I_m^{L,R}(t)$), *i.e.*, for different values of $\sigma(0)$. For the ML-MCTDH-SQR approach this amounts to selecting different initial single-particle wave functions for the system while, as pointed above, for the NEGF, the only term that depends on the initial electronic preparation of the system is $\mathcal{G}_0^<(0)$. It has been shown that for the extended Holstein model, the steady state values of σ are independent of the choice $\sigma(0)$ ²⁵, *i.e.*, the choice of $\mathcal{G}_0^<(0)$, but the dynamic response and relaxation to steady-state does depend on $\sigma(0)$.

We will also consider two different initial conditions for the phonons, one where $\delta_\alpha = 0$ in Eq. (31) corresponding to phonons initially equilibrated with an unoccupied dot, and another where $\delta_\alpha = 1$ corresponding to

phonons equilibrated to an occupied dot. Again, the description of these two initial conditions is rather simple within the ML-MCTDH-SQR approach and one selects the initial phonon wave function to correspond to one of these initial conditions. Within the NEGF formalism, this is a bit more delicate. The phonon initial condition enters the Kadanoff-Baym equations through the equilibrium lesser bare phonon GF, $\mathcal{D}_{0,\alpha}^<(0)$. For $\delta_\alpha = 0$ we set $\mathcal{D}_{0,\alpha}^<(0) = -\frac{i}{\hbar} (2n(\hbar\omega_\alpha) + 1)$, where $n(\omega) = \frac{1}{e^{\beta\hbar\omega} - 1}$ is the Bose-Einstein distribution.

For $\delta_\alpha = 1$ one can use a similar strategy and determine $\mathcal{D}_{0,\alpha}^<(0)$ according to Eq. (31). However, this would lead to large deviations of the NEGF approach from the numerically exact ML-MCTDH-SQR results, since this initial condition amounts to a situation where the phonons are equilibrated in the well corresponding to the occupied dot, a situation far from the perturbative regime about which the NEGF equations were derived. To resolve this and provide an equally accurate description of the NEGF-SCBA for the shifted phonon distribution, we propose to transform the phonon Hamiltonian in Eq.(4) by redefining a set of shifted ladder operators $\tilde{b}_\alpha = b_\alpha + \frac{M_\alpha}{\hbar\omega_\alpha}$ combined with particle/hole transformation $d \rightarrow \tilde{d}^\dagger, d^\dagger \rightarrow \tilde{d}$. With that, the shifted phonon Hamiltonian is given by:

$$H^{\delta=1} = (2\lambda - \varepsilon_d) \tilde{d}^\dagger \tilde{d} + \sum_{k \in L,R} \varepsilon_k a_k^\dagger a_k + \sum_\alpha \hbar\omega_\alpha \left(\tilde{b}_\alpha^\dagger \tilde{b}_\alpha + \frac{1}{2} \right) + \sum_{k \in L,R} \left(t_k \tilde{d}^\dagger a_k^\dagger + t_k^* \tilde{d} a_k \right) - \tilde{d}^\dagger \tilde{d} \sum_\alpha M_\alpha \left(\tilde{b}_\alpha^\dagger + \tilde{b}_\alpha \right), \quad (32)$$

which is identical to the phonon Hamiltonian in Eq.(4) with $\varepsilon_d \rightarrow 2\lambda - \varepsilon_d$ and $M_\alpha \rightarrow -M_\alpha$. Thus, one can adopt the NEGF-SCBA equations derived above with parameters reflecting this transformation. The initial condition for the shifted phonons will now correspond to $\langle \tilde{d}^\dagger \tilde{d} \rangle = 0$. In practice we use the NEGF-SCBA equations for both initial conditions of the phonons with the original set of parameters and $\mathcal{D}_{0,\alpha}^<(0) = -\frac{i}{\hbar} (2n(\hbar\omega_\alpha) + 1)$ for $\delta_\alpha = 0$ and with $\varepsilon_d \rightarrow 2\lambda - \varepsilon_d$, $M_\alpha \rightarrow -M_\alpha$ for $\delta_\alpha = 1$ with the same values for $\mathcal{D}_{0,\alpha}^<(0)$.

In Fig. 3 we compare the short-time behavior of the RDM obtained from the NEGF-SCBA to the numerically converged ML-MCTDH-SQR approach. Four initial preparations of the system were considered at different values of λ and ω_c . The agreement between the NEGF-SCBA and the ML-MCTDH-SQR results is remarkable even slightly outside the perturbative regime by which the SCBA is expected to fail, *i.e.*, for $\lambda/\Gamma > 1$.⁵⁰ While the ML-MCTDH-SQR is limited to times of the order of $35 \frac{\hbar}{\Gamma}$ the NEGF-SCBA can be used (within our computational resources) to times of the order of $100 \frac{\hbar}{\Gamma}$, which as shown below, is necessary to converge the RDM to steady-state for certain parameters. We note in pass-

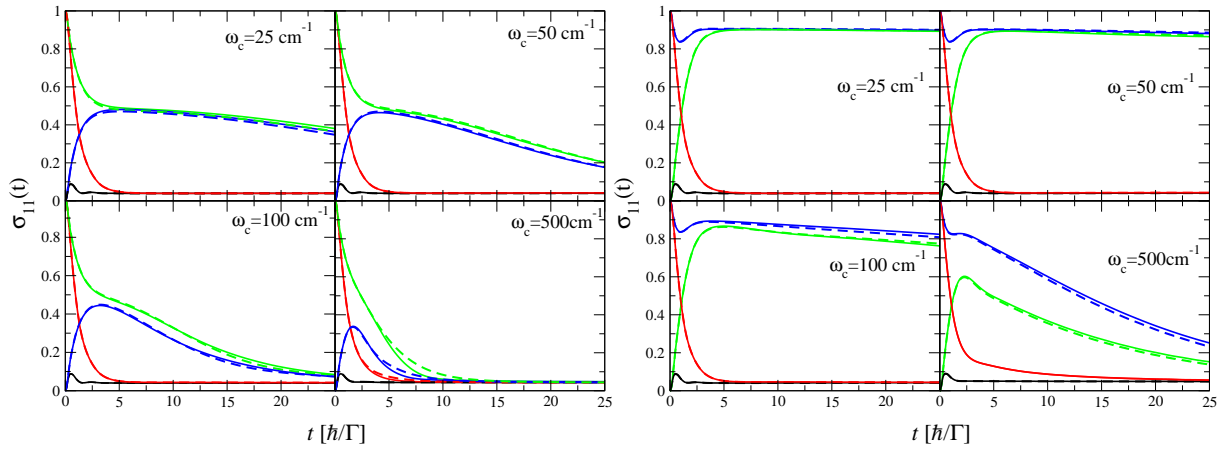


Figure 3: Comparison of the dot population ($\sigma_{11}(t)$) obtained from the ML-MCTDH-SQR (solid lines) and NEGF-SCBA (dashed lines) approaches for $\varepsilon_d/\Gamma = \frac{25}{8}$, $\lambda/\Gamma \approx 1.5$ (left panels) and $\lambda/\Gamma \approx 2.3$ (right panels), for frequencies in the range of $25 - 500 \text{ cm}^{-1}$ ($\approx 0.02 - 0.4$ in units of Γ/\hbar). The different curves correspond to different initial conditions: Black - unoccupied with $\delta_\alpha = 0$, Red - occupied with $\delta_\alpha = 0$, Blue - unoccupied with $\delta_\alpha = 1$ and Green - occupied with $\delta_\alpha = 1$.

ing that for values of $\lambda/\Gamma > 3$ we find that the NEGF-SCBA shows a pronounced deviation from the numerically converged results and thus can only provide a qualitative picture. However, for $\lambda/\Gamma < \frac{5}{2}$ it seems safe to use the NEGF-SCBA approach.

III. ANALYSIS OF THE NONEQUILIBRIUM DYNAMICS AT DIFFERENT TIME SCALES

The nonequilibrium dynamics of the quantum dot, represented by the RDM, exhibits various timescales, which are analyzed in this section using the approaches introduced above. We first consider the dynamics for relatively short times, *i.e.*, on timescales characterized by the dot-lead coupling ($\tau_\ell \approx \frac{\hbar}{\Gamma}$) and the typical phonon frequency $\tau_{\text{ph}} \approx \frac{1}{\omega_c}$. We show that the appearance of rapid decays of the RDM to steady state depends also the specific model parameters, in particular whether the coupling to the phonons shifts the energy of the dot in or out of the bias window, which is defined by the chemical potentials of the two leads. Next, we study the long-time decay of the RDM to steady state and address both the adiabatic ($\hbar\omega_c \ll \Gamma$) and non-adiabatic limits. In all results presented below, we consider the low temperature limit ($T = 0$).

A. Short and intermediate time scales

In Fig. 4, we plot the average dot population given by the diagonal occupied element of the RDM ($\sigma_{11}(t)$) for several typical phonon frequencies, for two values of the reorganization energy, $\lambda/\Gamma \approx \frac{3}{4}$ (lower panel) and $\lambda/\Gamma \approx \frac{3}{2}$ (upper panel), for $\mu_L = -\mu_R \approx \frac{1}{3}\Gamma$. As shown above, this regime of electron-phonon coupling is well suited for the two-time NEGF-SCBA combined with the

RDM formalism. We consider four different initial preparations of the dot and phonon density matrices: Occupied/empty dot where $\sigma(0) = \begin{pmatrix} 0 & 0 \\ 0 & 1 \end{pmatrix}$ for an occupied

dot and $\sigma(0) = \begin{pmatrix} 1 & 0 \\ 0 & 0 \end{pmatrix}$ otherwise, and shifted/unshifted phonons with $\delta_\alpha = 1, 0$, respectively. In all cases shown, the dot population decays to the same steady-state value, regardless of the initial preparation of the dot/phonons. For the case of $\delta_\alpha = 0$ (black and red curves) we find that the dynamics are characterized by a single timescale governed by $\tau_\ell \approx \frac{\hbar}{\Gamma}$. For $\delta_\alpha = 1$ (blue and green curves), this initial transient is followed by a decay on timescales of $\tau_{\text{ph}} \approx \frac{1}{\omega_c}$ for the larger reorganization energy (upper panels) while for $\lambda/\Gamma \approx \frac{3}{4}$ the phonon frequency is not always noticeable (lower panels). For higher values of λ not shown in Fig. 4, the picture will reverse, namely, dynamics on timescales of τ_{ph} will appear for an initially unshifted phonon distribution.

To better understand the intermediate time behavior, we provide a sketch of the two diabatic potential energy surfaces for a typical phonon frequency of $\omega_c = 100 \text{ cm}^{-1}$ for the two values of λ . For each plot, we also indicate the sum of dot and phonon energy of the 4 different initial conditions. It is quite clear that the most stable configuration is that of an empty dot with an unshifted phonon ($\delta_\alpha = 0$), which for small bias-voltages, would likely be the steady-state configuration. Therefore, regardless of the value of λ , when the system initial phonon distribution corresponds to the unshifted case (black and red curves), the phonons are already close to their steady-state distribution and the dynamics of the RDM are governed by the electronic decay determined by the coupling to the leads (Γ).

Considering the case of $\lambda/\Gamma = \frac{3}{2}$ for the shifted initial phonon distribution, at short times (τ_ℓ) the population of the dot decreases or increases to a value of $\frac{1}{2}$,

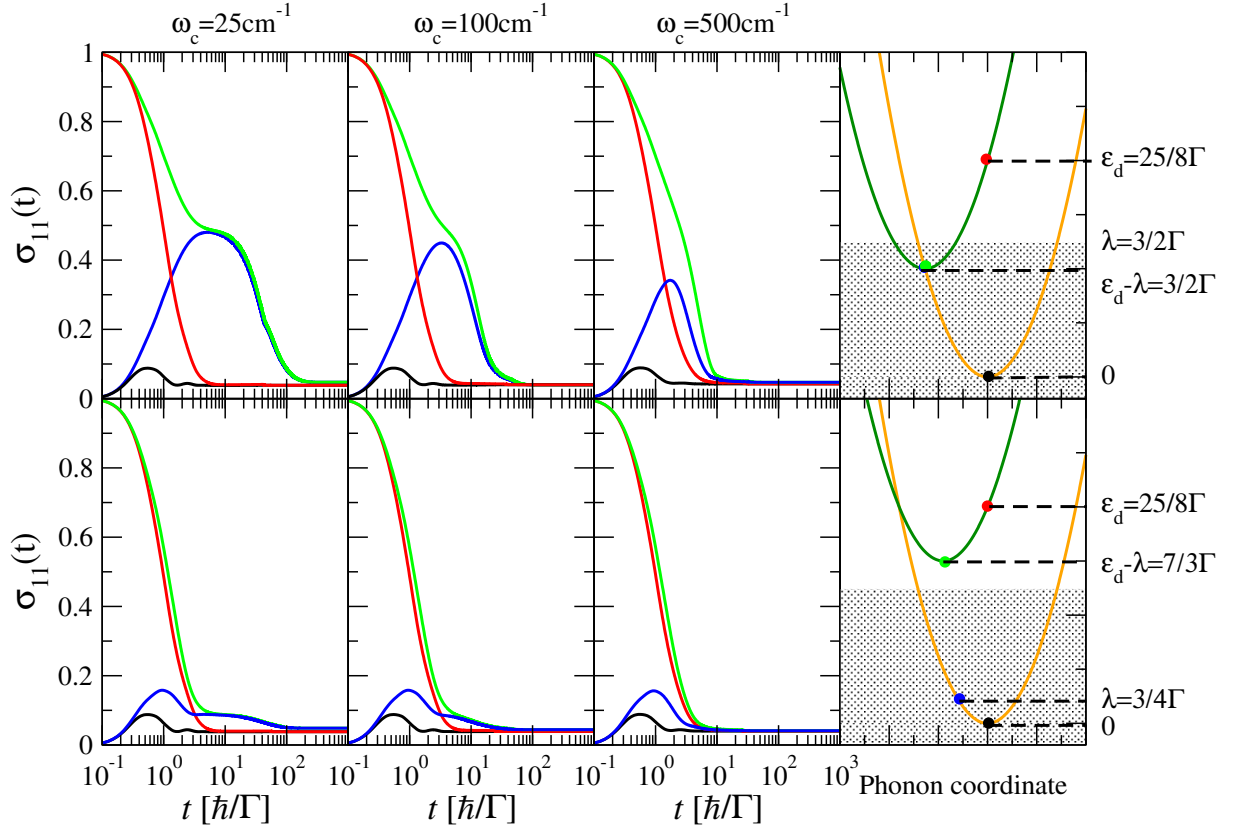


Figure 4: Left matrix-panels: Dot population ($\sigma_{11}(t)$) obtained from the RDM combined with the NEGF-SCBA for $\lambda/\Gamma = \frac{3}{2}$ (upper row panels) and $\lambda/\Gamma = \frac{3}{4}$ (lower row panels) for frequencies in the range of 25 – 500 cm^{-1} ($\approx 0.02 - 0.4$ in units of Γ/\hbar). Black, red, blue, and green curves correspond to unoccupied / occupied and $\delta_\alpha = 0 / \delta_\alpha = 1$, respectively. Right column-panels: Schematic sketch of the diabatic harmonic potential energy surfaces of the neutral (orange) and charged (green) state for the two values of λ . The marked values to the right label the dot and phonon minimum energy corresponding to each of the four initial condition. For each initial condition, we label the minimum energy with a solid circle with matching colors. Shaded area corresponds to the applied source-drain bias.

depending on whether the dot was occupied or empty initially, respectively. To understand this, we define the instantaneous difference in energy between an occupied and empty dot as $\delta\varepsilon$. For $x = 0$ (the minimum of the unshifted well) $\delta\varepsilon = \varepsilon_d$ and for $x = -\sqrt{2}\frac{M}{\hbar\omega_c}$ (the minimum of the shifted well) $\delta\varepsilon = \varepsilon_d - 2\lambda$. Returning to the case $\lambda/\Gamma = \frac{3}{2}$ for the shifted initial phonon distribution, $\delta\varepsilon = \varepsilon_d - 2\lambda \approx 0$ is nearly at the symmetric point about the bias window of conduction. Thus, freezing the phonons would lead to a steady-state population close to $\frac{1}{2}$, which is indeed observed for times $\tau_\ell < t < \tau_{\text{ph}}$ where the dot population levels at $\approx \frac{1}{2}$. The phonons, of course, are not frozen and as the system relaxes to the more stable well on timescales given by τ_{ph} . During this process, the instantaneous value of $\delta\varepsilon$ shifts above the bias conduction windows, resulting in a decay of the dot population.

For the smaller reorganization energy ($\lambda/\Gamma = \frac{3}{4}$) the energy difference $\delta\varepsilon$ is well above the bias window of conduction, and thus, the population of the dot never levels at values typical of resonance situations. Inevitably, the

system will relax to the more stable well corresponding to $\delta_\alpha = 0$ on a timescale τ_{ph} . Whether this appears in the dynamics of the RDM depends on the value of the dot population. For non-vanishing $\sigma_{11}(t)$, a clear signature of τ_{ph} is still evident.

The picture that emerges is rather simple. At short times, the dynamics of the RDM is always characterized by the coupling to the leads as long as $\hbar\omega_c < \Gamma$. The appearance of an additional timescale (τ_{ph}) depends on whether the phonons are initial equilibrated at the more stable well or not, and also whether the instantaneous energy difference between the occupied and empty dot passes through the bias conduction window as the system relaxes to steady-state. To further support this we show in Fig. 5 results for the dot population for different values of ε_d and a higher bias voltage $\mu_L = -\mu_R \approx \frac{2}{3}\Gamma$, for the same values of λ . The two left panels show results for $\varepsilon_d = 0$ in which the shifted well is the more stable one. As clearly evident, the role of the different initial conditions is reversed and the dynamics of the RDM corresponding to the shifted initial condition relax rapidly to the steady-state while the case of the unshifted initial

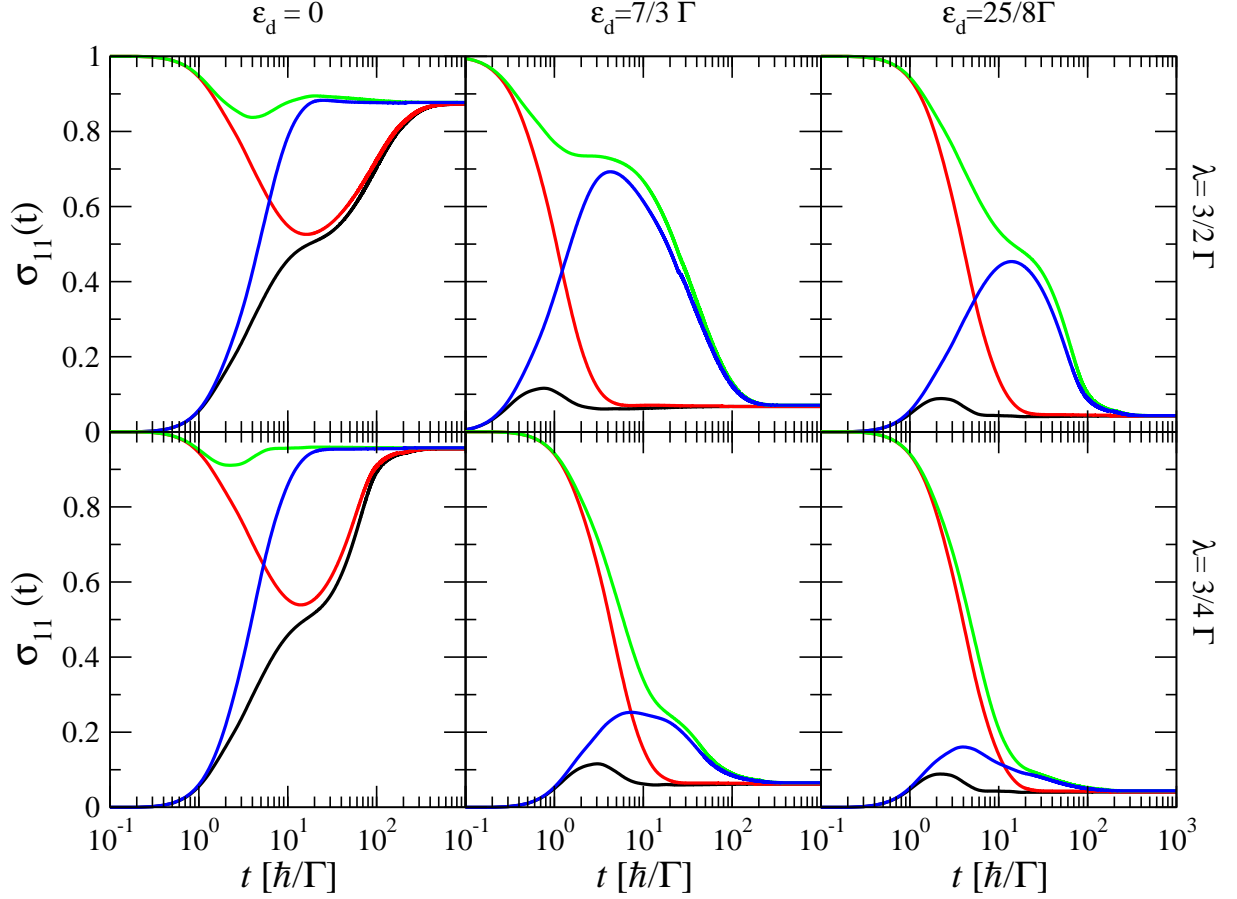


Figure 5: Dot population ($\sigma_{11}(t)$) obtained from the RDM combined with the NEGF-SCBA for $\omega_c = 100\text{cm}^{-1} \approx 0.08\Gamma/\hbar$. Black, red, blue, and green curves correspond to unoccupied / occupied and $\delta_\alpha = 0$ / $\delta_\alpha = 1$, respectively.

condition show intermediate transient behavior (with dot population approaching $\frac{1}{2}$ since $\delta\varepsilon = 0$ for this case) with a characteristic timescale τ_{ph} .

The case of $\varepsilon_d = \frac{7}{3}\Gamma$ and $\lambda = \frac{3}{2}\Gamma$ is special since $\delta\varepsilon = \varepsilon_d - 2\lambda = -\frac{2}{3}\Gamma$ equals to the lower conduction edge ($\mu_R = -\frac{2}{3}\Gamma$). As the system relaxes to the stable well the instantaneous value of $\delta\varepsilon$ scans the entire bias conduction window and the population of the dot increases above $\frac{1}{2}$, as it should for asymmetric resonant situations. When $\delta\varepsilon$ increases above the upper conduction edge, the dot population decreases with a typical timescale equal to τ_{ph} . This increase of the dot population above $\frac{1}{2}$ is not observed for $\lambda = \frac{3}{4}\Gamma$, since for this case $\delta\varepsilon = \frac{5}{6}$ is slightly above the upper conduction edge, and the system is never at resonance throughout the dynamics. This explains the lower values of the dot population at intermediate times.

B. Dynamics on longer time scales induced by electron-phonon interaction

Next, we consider the dynamics on longer time scales, induced by the coupling between the electron and phonon degrees of freedom. In Fig. 6 we plot the dot population

for a range of values of ω_c and λ , and for the four different initial conditions discussed above. The results span the crossover between the adiabatic ($\hbar\omega_c \ll \Gamma$) to the non-adiabatic ($\hbar\omega_c \rightarrow \Gamma$) limits. The values of the reorganization energy chosen are somewhat above the perturbative regime ($\lambda/\Gamma > 3$) in which the NEGF-SCBA is accurate. Therefore, we obtain the input required to generate the memory kernel and the RDM from the ML-MCTDH-SQR approach. In all cases shown, we used a cutoff time $t_c \approx 25\frac{\hbar}{\Gamma}$, sufficient to converge the rate of decay of the RDM at long times. The value of the steady state obtained from the cutoff approximation for these results, however, is not converged within the maximal cutoff time used of $t_c \approx 35\frac{\hbar}{\Gamma}$, which implies that there maybe a longer timescale by which the system relaxes.

The two left column-panels of Fig. 6 show results for slow phonons ($\omega_c \leq 100\text{cm}^{-1} \approx 0.08\Gamma/\hbar$), i.e. in the adiabatic regime. For the specific choice of parameters, we find that the long-time limit of the dot population depends on the initial phonon distribution but not on the initial dot occupation. The difference between the long-time plateau solutions diminishes as the phonon frequency increases, and will eventually vanish at the crossover to the non-adiabatic limit. The depen-

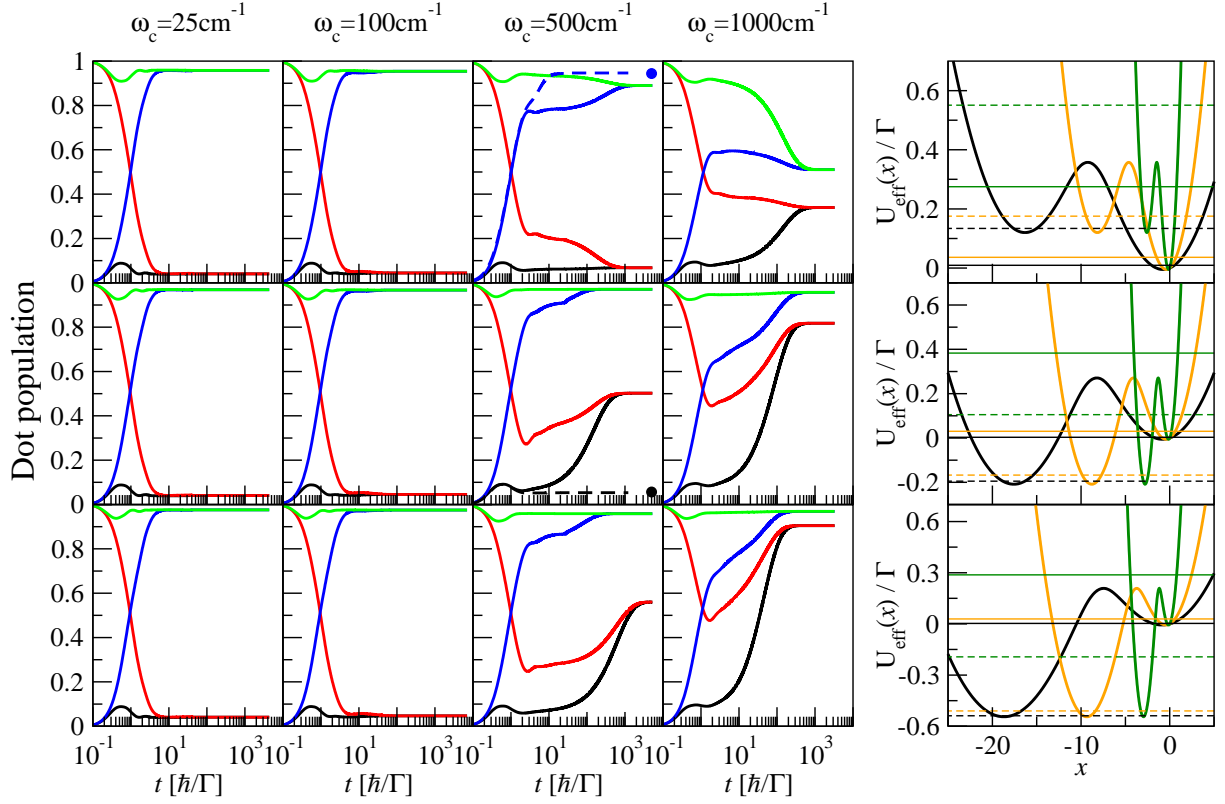


Figure 6: Left matrix-panels: Dot population obtained from the RDM formalism combined with the ML-MCTDH-SQR approach for $\lambda/\Gamma = 3.1$ (upper row panels), $\lambda/\Gamma = 3.5$ (middle row panels), and $\lambda/\Gamma = 3.9$ (lower row panels) for frequencies in the range of $25 - 1000 \text{ cm}^{-1}$ ($\approx 0.02 - 0.8$ in units of Γ/\hbar). Black, red, blue, and green curves correspond to unoccupied / occupied and $\delta_\alpha = 0$ / $\delta_\alpha = 1$, respectively. Dashed curves were obtained from the RDM formalism combined with the NEGF-SCBA and the solid circles are the NEGF-SCBA steady-state values. Right column panels: The effective potentials corresponding to each value of λ . Black, orange and deep green curves are for $\omega_c = 25, 100$, and 1000 cm^{-1} , respectively. The horizontal solid and dashed lines represent the ground state energy of the right and left well, respectively.

dence of the dot occupation for long times on the initial state suggests the existence of bistability. This bistability has been the subject of our recent study²⁵ and previous work^{3,33,65}. It will be addressed briefly later in this section and in more detail in section IV.

Concerning the dynamics, we find that in the adiabatic limit the RDM decays rapidly to a plateau, with a value that depends on the initial phonon distribution. The RDM decay is characterized by a single timescale, τ_ℓ , determined by the coupling to the leads. The existence of the plateau and the plateau value are insensitive to further increasing the cutoff time up to the limit of the ML-MCTDH-SQR approach, which is $t_c \approx 35 \frac{\hbar}{\Gamma}$. A significantly different behavior is observed for $\omega_c \geq 500 \text{ cm}^{-1} \approx 0.4\Gamma/\hbar$, which is near the crossover to the non-adiabatic limit. While the short time dynamics are very similar and are governed by the coupling to the leads with a time scale τ_ℓ , a pronounced long time decay is observed and then the system levels at a plateau. We note in passing that a similar long time decay has been reported by Albrecht *et al.*³⁵ for a single-phonon Holstein model (rather than a bath of phonons), using an NEGF approach within a quasi-adiabatic, single-time approxi-

mation. The results shown in Fig. 6 are based on a numerically exact formalism, and are therefore, free of any approximation or bias.

To understand the long time behavior in the adiabatic limit, we have calculated the adiabatic tunneling times as well as the transition probabilities for an effective adiabatic potential sketched in the right column-panels of Fig. 6. The effective potential,

$$U_{\text{eff}}(x) = U(x) + \int_{-\infty}^x dy n(y) \frac{d\varepsilon(y)}{dy} \quad (33)$$

is given as a sum of the bare potential $U(x) = \frac{\hbar}{2}\omega_c x^2$ and the potential of mean force, $\int_{-\infty}^x dy n(y) \frac{d\varepsilon(y)}{dy}$. Here, $\varepsilon(x) = \varepsilon_d + \sqrt{2}M_c x$ is the unweighted instantaneous dot energy and

$$n(x) = \int \frac{d\omega}{\pi} \frac{\Gamma_L(\omega) f_L(\omega) + \Gamma_R(\omega) f_R(\omega)}{(\omega - \varepsilon(x))^2 + \Gamma^2(\omega)} \quad (34)$$

is the average, out-of-equilibrium, dot population valid for the adiabatic limit⁶⁶. We find that the adiabatic tun-

neling times for $\omega_c = 25\text{cm}^{-1}$ and $\omega_c = 100\text{cm}^{-1}$ are of the order of $1500\frac{\hbar}{\Gamma}$ and $150\frac{\hbar}{\Gamma}$, respectively and the tunneling probabilities are smaller than 10^{-5} . For the former case ($\omega_c = 25\text{cm}^{-1}$) one may argue that this timescale is too long to be captured by the RDM formalism with a cutoff time of $t_c \approx 35\frac{\hbar}{\Gamma}$ and perhaps, for larger cutoff times which are not accessible to us, the RDM will decay due to tunneling between the two wells. However, this argument seems much less likely for $\omega_c = 100\text{cm}^{-1}$, where the tunneling time is much smaller ($150\frac{\hbar}{\Gamma}$), and thus, tunneling should be captured even with cutoff times of the order of $t_c \approx 35\frac{\hbar}{\Gamma}$.

The fact that we do not observe any long time relaxation to a unique steady state in the adiabatic limit is consistent with the notion that tunneling is suppressed by the dynamical coupling to the phonons, which was assumed static in the above estimation of the tunneling process. Additionally, the low tunneling probability may also be used to explain the vanishing long time transient behavior in the adiabatic limit. To further elaborate on this and to elucidate the underlying time scales and mechanisms, we have considered the simpler scenario of the decay of an initially occupied dot state coupled only to the unoccupied states in the right lead, *i.e.* the states above the chemical potential of the right electrode. This simplified version of the Anderson-Newns model of heterogeneous electron transfer reduces dramatically the computational complexity of the ML-MCTDH-SQR calculations and allows us to directly access times that are of the order or longer than the adiabatic tunneling times. In the upper panel of Fig. 7 we show the population dynamics corresponding to this case for $\omega_c = 100\text{cm}^{-1}$ and $\lambda/\Gamma = 2.7$, for an initially occupied dot and shifted phonon distribution ($\delta_\alpha = 1$). We consider both a single phonon mode and an Ohmic bath. The estimated adiabatic tunneling time on $U_{\text{eff}}(x)$ for this case is $300\frac{\hbar}{\Gamma}$. The results for a single phonon mode show relaxation of the dot population on timescales exceeding $10^3\frac{\hbar}{\Gamma}$, which indicate that the dynamical coupling to a single mode increases the tunneling time between the two wells compared with the pure adiabatic limit. For the Ohmic bath, the dot population is stable even on times approaching $10^4\frac{\hbar}{\Gamma}$ and tunneling is not observed, suggesting stronger localization. This localization can be understood in term of the reaction mode representation of the phonons, which for an Ohmic bath corresponds to an over-damped oscillator.^{67–69} Whether localization will suppress tunneling even at longer times remains an open problem.

The lower panel of Fig. 7 shows the results for the same simplified Anderson-Newns model, but for $\omega_c = 500\text{cm}^{-1} \approx 0.4\Gamma/\hbar$, which is near the adiabatic/non-adiabatic crossover. The remaining parameters are the same as those shown in the upper panel of Fig. 7 for $\omega_c = 100\text{cm}^{-1} \approx 0.08\Gamma/\hbar$. The dot population shows a two-step relaxation even for the Ohmic case, eventually, relaxing to zero. The analysis shows that the longer time decay can be associated with a non-adiabatic tran-

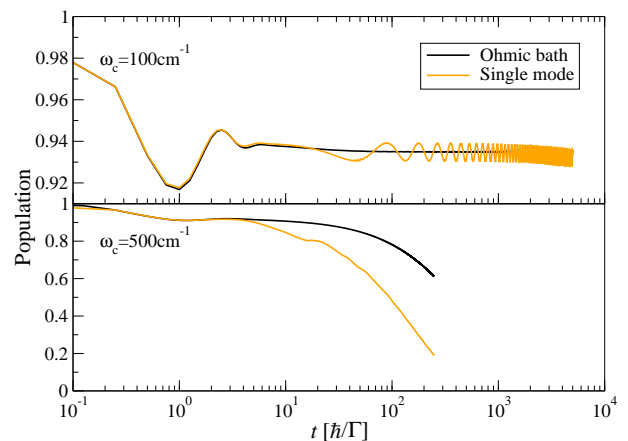


Figure 7: Dynamics of the dot population for an initially occupied bridge state coupled to a single lead and a single phonon (orange) or an Ohmic bath (black), for $\varepsilon_d/\Gamma = \frac{25}{8}$, $\lambda/\Gamma = 2.7$, and a bias of $\frac{5}{8}\Gamma$.

sition, with a time constant that can be approximated by $\tau_{\text{na}} \approx \frac{\hbar}{\Gamma} e^{\lambda/\hbar\omega_c}$ for the single-mode case.^{35,70} Comparing the single-mode to the Ohmic case reveals that the non-adiabatic transition is much slower for the latter. This behavior is similar to the dynamics of the population in the adiabatic limit, which showed vanishing tunneling for the Ohmic case.

By analogy, we can associate the long-time decay of the full extended Holstein model with two leads (right column-panels of Fig. 6) to a non-adiabatic transition from the occupied to the unoccupied state. Despite the fact that the dot population does not decay to zero, the timescales and behavior are similar to the single-lead case, and the decay rate scales roughly as $e^{-\lambda/\hbar\omega_c}$. Interestingly, the non-adiabatic transition does not destroy the bistability (in some cases). This is rather surprising, but also very significant. Despite having transitions between the two diabatic surfaces, the long time limit plateau of the RDM still depends on the initial phonon distribution! We note in passing that the NEGF-SCBA approach does not describe the non-adiabatic process (dashed curves in Fig. 6), and therefore, does not show any long time transient behavior in this parameter regime.

IV. SIGNATURES OF BISTABILITY

We have shown previously that the value of the RDM at steady state is independent of the initial occupation of the dot, *i.e.* on the initial state of the electronic degrees of freedom.²⁵ The proof is rather simple and is based on the Laplace final value theorem which relates $\sigma(t \rightarrow \infty)$ to the integral of the memory kernel, $\mathcal{K} = \frac{1}{\hbar^2} \int_0^\infty d\tau \kappa(\tau)$. Indeed, for all the results shown above, the long time limit of the RDM is independent of the initial dot occupation, as it should be. However, for certain model param-

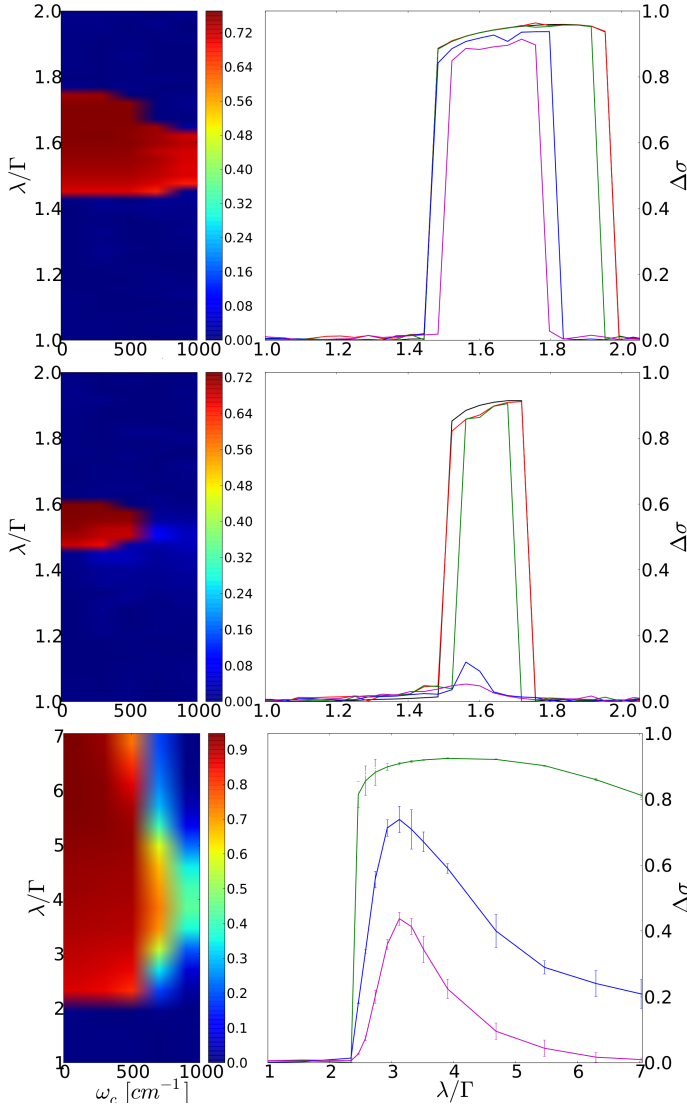


Figure 8: A plot of the value of the bistability, $\Delta\sigma$, as a function of λ and ω_c . Upper, middle and lower panels are for $\varepsilon_d/\Gamma = \frac{25}{16}$ and $\mu_L - \mu_R = 0$, $\varepsilon_d/\Gamma = \frac{25}{16}$ and $\mu_L - \mu_R = \frac{5}{8}\Gamma$, and $\varepsilon_d/\Gamma = \frac{25}{8}$ and $\mu_L - \mu_R = \frac{5}{8}\Gamma$, respectively. The upper two panels were generated by the steady-state NEGF-SCBA approach. For the lower panel, the steady-state NEGF-SCBA was used for $\lambda/\Gamma \leq 2\frac{1}{3}$ and ML-MCTDH-SQR combined with the RDM otherwise. Black, red, dark green, blue and magenta show results for $\omega_c = 25, 50, 100, 500$ and 1000 cm^{-1} ($\approx 0.02, \approx 0.04, \approx 0.08, \approx 0.4$ and ≈ 0.8 in units of Γ/\hbar) respectively.

eters, we find (and also others^{3,25,29,32,33,71}) that the long time value of the RDM can depend on the initial preparation of the phonon degrees of freedom. This finding suggests the existence of bistability in the system. The value of the population difference of the two initial phonon preparation, $\Delta\sigma = \sigma_{11}^{\delta_\alpha=1}(t \rightarrow \infty) - \sigma_{11}^{\delta_\alpha=0}(t \rightarrow \infty)$ for long times is a measure of the importance of bistability, and will in the following be referred to simply as bistability. In the current section, we analyze the dependence

of bistability on the various model parameters.

In Fig. 8 we plot the results for $\Delta\sigma$ for two values of the dot energy ε_d and the bias voltage $\Delta\mu = \mu_L - \mu_R$, and for a range of frequencies (ω_c) and reorganization energies (λ). The upper two panels correspond to $\varepsilon_d/\Gamma = 25/16$. In this case, the results were generated using the steady-state NEGF-SCBA and thus, the approach is limited to relatively low values of λ . Note, however, that bistability is not observed for $\lambda/\Gamma > 2$, which is exactly the regime where NEGF-SCBA is accurate, as shown above (cf., Fig. 3). In fact, comparing the dynamics for one of the values of ω_c generated by the NEGF-SCBA with the numerically converged ML-MCTDH-SQR for which $\Delta\sigma \neq 0$ indicates excellent agreement (data not shown here) even for $\varepsilon_d/\Gamma = 25/16$.

In the lower panel of Fig. 8 we show results for $\varepsilon_d/\Gamma = 25/8$ and $\Delta\mu = \frac{5}{8}\Gamma$. Here, the results were generated by the ML-MCTDH-SQR approach combined with the RDM formalism and thus, are not limited to small values of λ . In most cases, we used a cutoff time $t_c \leq 35 \frac{\hbar}{\Gamma}$. This cutoff time was not always sufficient to converge the long time values of the RDM. In the upper panel of Fig. 9 we illustrate this for a case where $\Delta\sigma = 0$ and for a sufficiently small value of λ so that the ML-MCTDH-SQR results can be compared with the NEGF-SCBA. For the initial condition corresponding to $\delta_\alpha = 0$ (black curves), we find that the values of the RDM are insensitive to the cutoff time for $t_c \geq 10 \frac{\hbar}{\Gamma}$. This is expected, since the steady state of the system is close to the initial condition $\delta_\alpha = 0$ and thus, the phonons are nearly at steady state initially. This is not the case for the other initial condition corresponding to $\delta_\alpha = 1$ (blue curves). As $\frac{1}{t_c}$ decreases the dot population decreases and never levels off. In fact, the steady-state value of the dot population obtained from the steady-state NEGF-SCBA is rather small and equals that value for $\delta_\alpha = 0$ (i.e., $\Delta\sigma = 0$). In this case, it seems that a much larger cutoff time is needed to converge the RDM in this case, even larger than the limit of the two-time NEGF-SCBA which is $t_c \approx 100 \frac{\hbar}{\Gamma}$.

The middle panel of Fig. 9 shows results for a relatively small coupling parameter for which the ML-MCTDH-SQR results can be compared with those of the NEGF-SCBA approach. Again, for $\delta_\alpha = 0$, a rather small cutoff time is sufficient to converge the results since the phonon initial density matrix is close to its steady-state value. The case of $\delta_\alpha = 1$ requires a much larger cutoff time. In fact, larger than the computational limit of the ML-MCTDH-SQR approach, but still within the reach of the two-time NEGF-SCBA, for which a clear plateau is observed as $\frac{1}{t_c}$ decreases. The plateau value agrees well with the steady-state NEGF-SCBA calculation (solid circle). Situations of this sort are considered converged.

In the lower panel of Fig. 9 we show results for a large value of $\lambda/\Gamma > 3$, and thus, only the ML-MCTDH-SQR was used to obtain the RDM. Here, the well corresponding to $\delta_\alpha = 1$ is the more stable one, and therefore, it is rather easy to converge the dot population for this initial condition (blue curve). For the other initial condition, a

clear leveling of the dot population as $\frac{1}{t_c} \rightarrow 0$ is evident. However, the value of the steady-state is quite noisy due to computational limitations of the ML-MCTDH-SQR method. Situations of this sort, for which we observe the beginning of the leveling of the dot population as t_c is increased to the computational limit, will be considered converged. However, to indicate the fact that the long time limit of the dot population is noisy, we assign a large error bar of the size of the fluctuations to the value of $\Delta\sigma$ shown in Fig. 8.

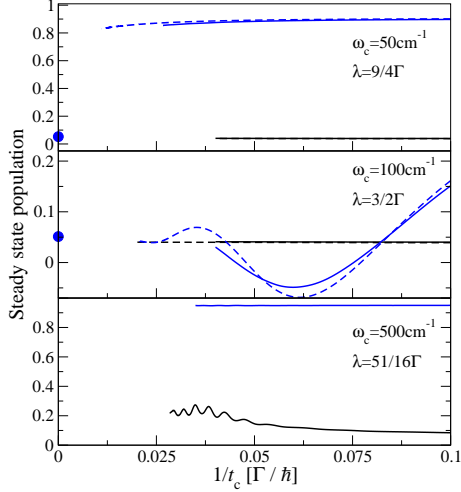


Figure 9: The steady-state dot population as a function of $1/t_c$. Solid and dashed curves are results obtained by the ML-MCTDH-SQR and NEGF-SCBA combined with the RDM formalism, respectively. The black and blue lines are results for $\delta_\alpha = 0$ and 1, respectively. The solid circle is the steady-state NEGF-SCBA result. $\varepsilon_d/\Gamma = \frac{25}{8}$ for all panels.

Returning to discuss the results of Fig. 8 within the above limitations concerning the convergence of the results, several important conclusions can be drawn:

- As the source-drain bias voltage V increases the window of bistability decreases and will eventually disappear.³ It is important to note, however, that we find a finite value for $\Delta\sigma$ on timescales much longer than $\frac{\hbar}{\Delta\mu}$. A similar effect is expected if the temperature is increased.
- The window of bistability also decreases as the dot energy ε_d decreases. For the adiabatic limit, this is strongly correlated with the range of reorganization energies, λ , for which the effective potential of the phonons shows a distinct double-well structure. This range decreases with ε_d .
- As ω_c increases the window of bistability decreases and so does the value of $\Delta\sigma$. Surprisingly, however, even for relatively large values of $\hbar\omega_c \approx \Gamma$ away from the adiabatic limit, we still observe bistability.

In the adiabatic limit, the first two findings can be rationalized by the already mentioned fact that a precondition

for bistability is the existence of an effective potential for the phonons with two stable minima, which have to have energies outside the bias window, *i.e.* $\varepsilon_d - 2\lambda \ll \mu_{L/R} \ll \varepsilon_d$ and $\Gamma, V \ll \lambda$ (see also the discussion in Refs. 3 and 65). The most striking result is that the phenomenon of bistability exists away from the strictly adiabatic limit and prevails on time scales longer than the non-adiabatic transition time, *i.e.* on much longer time scales than previously thought.³³ The question remains, however, whether bistability in the extended Holstein model exists in the strict long-time limit. The unambiguous clarification of this question requires a numerically exact methodology which can address directly the long-time limit of this model, which is yet to be developed.

V. CONCLUDING REMARKS

In this paper, we have investigated the nonequilibrium quantum dynamics of the extended Holstein model as a generic model for charge transport in a quantum dot with electron-phonon interactions. We have specifically focused on the transient dynamics and the approach to steady-state. To this end, we have used a methodology, which combines a reduced density matrix formalism based on projection-operator techniques and two different approaches to calculate the memory kernel, a two-time NEGF with the SCBA and the ML-MCTDH-SQR. The latter method provides a numerically exact treatment of the many-body quantum dynamics up to a certain time.

The results obtained in a wide range of parameters reveal dynamics on multiple timescales. In addition to the short and intermediate timescales associated with the separate electronic and phononic degrees of freedom, the electron-phonon coupling introduces longer timescales related to the adiabatic or nonadiabatic tunneling between the two charge states. The analysis shows, furthermore, that the value of the dot occupation may depend on the initial preparation of the phonon degrees of freedom, suggesting the existence of bistability. Intriguingly, the phenomenon of bistability persists even on timescales longer than the adiabatic/nonadiabatic tunneling time. Considering different parameter ranges, we have formulated conditions for bistability. This analysis shows that bistability is particularly pronounced for low characteristic frequencies of the phonons and moderate to large electron-phonon couplings. On the other hand, bistability is quenched for larger voltages. A similar effect is expected for higher temperatures.

The present study, employing time-dependent methods, cannot address the strict long-time limit and, therefore, cannot give a final answer to the controversial question whether a unique steady-state always exists for the extended Holstein model. The results do show, however, a significant dependence on the initial state on timescales which are accessible by time-resolved spectroscopy and,

thus, should be experimentally observable.

VI. ACKNOWLEDGMENTS

EYW and ER would like to thank Tal Levy, Kristen Kaasbjerg and Robert van Leeuwen for insightful discussions. MT thanks Jeremy Richardson for helpful discussions. EYW is grateful to The Center for Nanoscience

and Nanotechnology at Tel Aviv University for a doctoral fellowship. HW acknowledges the support from the National Science Foundation CHE-1012479. This work was supported by the German Research Council (DFG) and used resources of the National Energy Research Scientific Computing Center, which is supported by the Office of Science of the U.S. Department of Energy under Contract No. DE-AC02-05CH11231, and the Leibniz Computing Center (LRZ) Munich.

-
- ¹ A. Feldman, M. Steigerwald, X. Guo, and C. Nuckolls, *Acc. Chem. Res.* **41**, 1731 (2008).
 - ² J. C. Cuevas and E. Scheer, *Molecular Electronics: An Introduction to Theory and Experiment* (World Scientific, Singapore, 2010).
 - ³ M. Galperin, M. A. Ratner, and A. Nitzan, *Nano Lett.* **5**, 125 (2005), ISSN 1530-6984.
 - ⁴ R. Leturcq, C. Stampfer, K. Inderbitzin, L. Durrer, C. Hierold, E. Mariani, M. Schultz, F. von Oppen, and K. Ensslin, *Nat. Phys.* **5**, 327 (2009).
 - ⁵ G. Granger, D. Taubert, C. Young, L. Gaudreau, A. Kam, S. Studenikin, P. Zawadzki, D. Harbusch, D. Schuh, W. Wegscheider, et al., *Nature Phys.* **8**, 522 (2012).
 - ⁶ A. Benyamini, A. Hamo, A. Kusminskiy, F. von Oppen, and S. Ilani, *Nature Phys.* **10**, 151 (2014).
 - ⁷ M. Galperin, M. A. Ratner, and A. Nitzan, *J. Phys.: Condens. Matter* **19**, 103201 (2007).
 - ⁸ N. P. de Leon, W. Liang, Q. Gu, and H. Park, *Nano Lett.* **8**, 2963 (2008).
 - ⁹ Z. Ioffe, T. Shamaï, A. Ophir, G. Noy, I. Yutsis, K. Kfir, O. Cheshnovsky, and Y. Selzer, *Nature Nanotech.* **3**, 727 (2008).
 - ¹⁰ D. R. Ward, N. J. Halas, J. W. Ciszek, J. M. Tour, Y. Wu, P. Nordlander, and D. Natelson, *Nano Lett.* **8**, 919 (2008).
 - ¹¹ R. Härtle, C. Benesch, and M. Thoss, *Phys. Rev. Lett.* **102**, 146801 (2009).
 - ¹² A. K. Hüttel, B. Witkamp, M. Leijnse, M. R. Wegewijs, and H. S. J. van der Zant, *Phys. Rev. Lett.* **102**, 225501 (2009).
 - ¹³ J. Repp and G. Meyer, *Nat. Phys.* **6**, 975 (2010).
 - ¹⁴ J. Hihath, C. Bruot, and N. Tao, *ACS Nano* **4**, 3823 (2010).
 - ¹⁵ S. Ballmann, W. Hieringer, D. Secker, Q. Zheng, J. A. Gladysz, A. Görling, and H. B. Weber, *Chem. Phys. Chem.* **11**, 2256 (2010).
 - ¹⁶ E. A. Osorio, M. Ruben, J. S. Seldenthuis, J. M. Lehn, and H. S. J. van der Zant, *Small* **6**, 174 (2010).
 - ¹⁷ C. Arroyo, T. Frederiksen, G. Rubio-Bollinger, M. Velez, A. Arnau, D. Sanchez-Portal, and N. Agrait, *Phys. Rev. B* **81**, 075405 (2010).
 - ¹⁸ D. Secker, S. Wagner, S. B. R. Härtle, M. Thoss, and H. B. Weber, *Phys. Rev. Lett.* **106**, 136807 (2011).
 - ¹⁹ R. Härtle and M. Thoss, *Phys. Rev. B* **83**, 125419 (2011).
 - ²⁰ Y. Kim, H. Song, F. Strigl, H.-F. Pernau, T. Lee, and E. Scheer, *Phys. Rev. Lett.* **106**, 196804 (2011).
 - ²¹ D. Ward, D. Corley, J. Tour, and D. Natelson, *Nat. Nanotechnol.* **6**, 33 (2011).
 - ²² S. Ballmann, R. Härtle, P. Coto, M. Elbing, M. Mayor, M. Bryce, M. Thoss, and H. B. Weber, *Phys. Rev. Lett.* **109**, 056801 (2012).
 - ²³ K. Albrecht, H. Wang, L. Mühlbacher, M. Thoss, and A. Komnik, *Phys. Rev. B* **86**, 081412(R) (2012).
 - ²⁴ S. Ballmann, W. Hieringer, R. Härtle, P. Coto, M. Bryce, A. Görling, M. Thoss, and H. B. Weber, *Phys. Status Solidi B* **250**, 2452 (2013).
 - ²⁵ E. Y. Wilner, H. Wang, G. Cohen, M. Thoss, and E. Rabani, *Phys. Rev. B* **88**, 045137 (2013).
 - ²⁶ R. Härtle, M. Butzin, and M. Thoss, *Phys. Rev. B* **87**, 085422 (2013).
 - ²⁷ R. Härtle, U. Peskin, and M. Thoss, *Phys. Status Solidi B* **250**, 2365 (2013).
 - ²⁸ A. Mitra, I. Aleiner, and A. Millis, *Phys. Rev. Lett.* **94**, 076404 (2005).
 - ²⁹ M. Galperin, A. Nitzan, and M. A. Ratner, *J. of Phys.: Condens. Matter* **20**, 374107 (2008).
 - ³⁰ A. S. Alexandrov and A. M. Bratkovsky, *J. Phys. Condens. Matter* **19**, 255203 (2007).
 - ³¹ A. S. Alexandrov and A. M. Bratkovsky, *Phys. Rev. B* **80**, 115321 (2009).
 - ³² A. A. Dzhioev and D. S. Kosov, *J. Chem. Phys.* **135**, 174111 (2011).
 - ³³ K. F. Albrecht, H. Wang, L. Mühlbacher, M. Thoss, and A. Komnik, *Phys. Rev. B* **86**, 081412 (2012).
 - ³⁴ A. O. Gogolin and A. Komnik, *arXiv* 0207513.
 - ³⁵ K. F. Albrecht, A. Martin-Rodero, R. C. Monreal, L. Mühlbacher, and A. Levy Yeyati, *Phys. Rev. B* **87**, 085127 (2013).
 - ³⁶ M. Leijnse and M. R. Wegewijs, *Phys. Rev. B* **78**, 235424 (2008).
 - ³⁷ G. Cohen and E. Rabani, *Phys. Rev. B* **84**, 075150 (2011).
 - ³⁸ G. Cohen, E. Y. Wilner, and E. Rabani, *New J. Phys.* **15**, 073018 (2013), ISSN 1367-2630.
 - ³⁹ H. Wang and M. Thoss, *J. Chem. Phys.* **119**, 1289 (2003).
 - ⁴⁰ H. Wang and M. Thoss, *J. Chem. Phys.* **131**, 024114 (2009).
 - ⁴¹ S. Kohler, J. Lehmann, and P. Hänggi, *Phys. Rep.* **406**, 379 (2005).
 - ⁴² G. Li, M. Schreiber, and U. Kleinekathöfer, *Europhys. Lett.* **79**, 27006 (2007).
 - ⁴³ G. Li, B. Fainberg, A. Nitzan, S. Kohler, and P. Hänggi, *Phys. Rev. B* **81**, 165310 (2010).
 - ⁴⁴ L. Mühlbacher and E. Rabani, *Phys. Rev. Lett.* **100**, 176403 (2008).
 - ⁴⁵ R. Hütten, S. Weiss, M. Thorwart, and R. Egger, *Phys. Rev. B* **85**, 121408(R) (2012).
 - ⁴⁶ L. Simine and D. Segal, *J. Chem. Phys.* **138**, 214111 (2013).
 - ⁴⁷ A. Jovchev and F. Anders, *Phys. Rev. B* **87**, 195112 (2013).
 - ⁴⁸ B. Kubala and F. Marquardt, *Phys. Rev. B* **81**, 115319 (2010).
 - ⁴⁹ M. Cizek, M. Thoss, and W. Domcke, *Phys. Rev. B* **70**,

- 125406 (2004).
- ⁵⁰ A. Mitra, I. Aleiner, and A. Millis, Phys. Rev. B **69**, 245302 (2004).
 - ⁵¹ J. Koch and F. von Oppen, Phys. Rev. Lett. **94**, 206804 (2005).
 - ⁵² C. Benesch, M. Cizek, J. Klimes, I. Kondov, M. Thoss, and W. Domcke, J. Phys. Chem. C **112**, 9880 (2008).
 - ⁵³ G. Cohen, E. Gull, D. R. Reichman, A. J. Millis, and E. Rabani, Phys. Rev. B **87**, 195108 (2013).
 - ⁵⁴ H.-D. Meyer, U. Manthe, and L. Cederbaum, Chem. Phys. Lett. **165**, 73 (1990).
 - ⁵⁵ H.-D. Meyer, F. Gatti, and G. Worth, *Multidimensional Quantum Dynamics: MCTDH Theory and Applications* (Wiley-VCH, Weinheim, 2009).
 - ⁵⁶ H. Wang, I. Pshenichnyuk, R. Härtle, and M. Thoss, J. Chem. Phys. **135**, 244506 (2011).
 - ⁵⁷ H. Wang and M. Thoss, J. Phys. Chem. A **117**, 7431 (2013).
 - ⁵⁸ H. Wang and M. Thoss, J. Chem. Phys. **138**, 134704 (2013).
 - ⁵⁹ A. P. Jauho, N. S. Wingreen, and Y. Meir, Phys. Rev. B **50**, 5528 (1994).
 - ⁶⁰ H. Haug and A.-P. Jauho, *Quantum kinetics in transport and optics of semiconductors*, Springer series in solid-state sciences, (Springer, Berlin ; New York, 2008), 2nd ed.
 - ⁶¹ G. Stefanucci and R. v. Leeuwen, *Nonequilibrium Many-Body Theory of Quantum Systems: A Modern Introduction* (Cambridge University Press, 2013), ISBN 9780521766173.
 - ⁶² L. P. Kadanoff and G. Baym, *Quantum Statistical Mechanics: Green's Function Methods in Equilibrium and Nonequilibrium Problems* (Perseus Books, 1994), ISBN 9780201410464.
 - ⁶³ P. Myöhänen, A. Stan, G. Stefanucci, and R. v. Leeuwen, J. Phys. Conf. Ser. **220**, 012017 (2010), ISSN 1742-6596.
 - ⁶⁴ Y. Meir and N. S. Wingreen, Phys. Rev. Lett. **68**, 2512 (1992).
 - ⁶⁵ D. Mozyrsky, M. Hastings, and I. Martin, Phys. Rev. B **73**, 035104 (2006).
 - ⁶⁶ D. S. Kosov, J. Chem. Phys. **131**, 171102 (2009), ISSN 0021-9606, 1089-7690.
 - ⁶⁷ M. Thoss, H. Wang, and W. H. Miller, J. Chem. Phys. **115**, 2991 (2001).
 - ⁶⁸ H. Wang and M. Thoss, New J. Phys. **10**, 115005 (2008).
 - ⁶⁹ U. Weiss, *Quantum Dissipative Systems* (World Scientific, Singapore, 1999).
 - ⁷⁰ E. Eidelstein, D. Goberman, and A. Schiller, Phys. Rev. B **87**, 075319 (2013).
 - ⁷¹ A. A. Dzhioev and D. S. Kosov, J. Chem. Phys. **135**, 074701 (2011).